

Ground-Optimized 4D Radar-Inertial Odometry via Continuous Velocity Integration using Gaussian Process

Wooseong Yang¹, Hyesu Jang² and Ayoung Kim^{1*}

Abstract—Radar ensures robust sensing capabilities in adverse weather conditions, yet challenges remain due to its high inherent noise level. Existing radar odometry has overcome these challenges with strategies such as filtering spurious points, exploiting Doppler velocity, or integrating with inertial measurements. This paper presents two novel improvements beyond the existing radar-inertial odometry: ground-optimized noise filtering and continuous velocity preintegration. Despite the widespread use of ground planes in LiDAR odometry, imprecise ground point distributions of radar measurements cause naive plane fitting to fail. Unlike plane fitting in LiDAR, we introduce a zone-based uncertainty-aware ground modeling specifically designed for radar. Secondly, we note that radar velocity measurements can be better combined with IMU for a more accurate preintegration in radar-inertial odometry. Existing methods often ignore temporal discrepancies between radar and IMU by simplifying the complexities of asynchronous data streams with discretized propagation models. Tackling this issue, we leverage GP and formulate a continuous preintegration method for tightly integrating 3-DOF linear velocity with IMU, facilitating full 6-DOF motion directly from the raw measurements. Our approach demonstrates remarkable performance (less than 1% vertical drift) in public datasets with meticulous conditions, illustrating substantial improvement in elevation accuracy. The code will be released as open source for the community: <https://github.com/wooseongY/Go-RIO>.

I. INTRODUCTION

Robot navigation using radars has experienced remarkable advancements for their resilient perception capabilities in challenging weather conditions [1–5]. Moreover, its capability of providing Doppler velocity distinguishes the radar sensor from the traditional sensors, leading to significant enhancements in visually degraded environments [6].

Despite the above advantages, radar measurements are vulnerable to false alarms and multipath reflections, thus necessitating outlier rejection. Among many existing methods, intensity-based filtering [7] and Constant False-Alarm Rate (CFAR) are the most widely utilized. However, these approaches are threshold-sensitive and can be limited in terms of generalizability. In this context, leveraging ground could be a feasible solution as it demonstrated its reliable noise filtering ability in Light Detection and Ranging (LiDAR) [8–13]. Unfortunately, naive plane fitting as in LiDAR would fail because of the inherent uncertainty and imprecise distribution in radar [14, 15].

¹W. Yang and A. Kim are with the Dept. of Mechanical Engineering, SNU, Seoul, S. Korea [yellowish, ayoungk@snu.ac.kr]

²H. Jang is with the Institute of Advanced Machines and Design, SNU, Seoul, S. Korea dortz@snu.ac.kr

This work was supported by the MOITE, Korea (No. 1415187329).

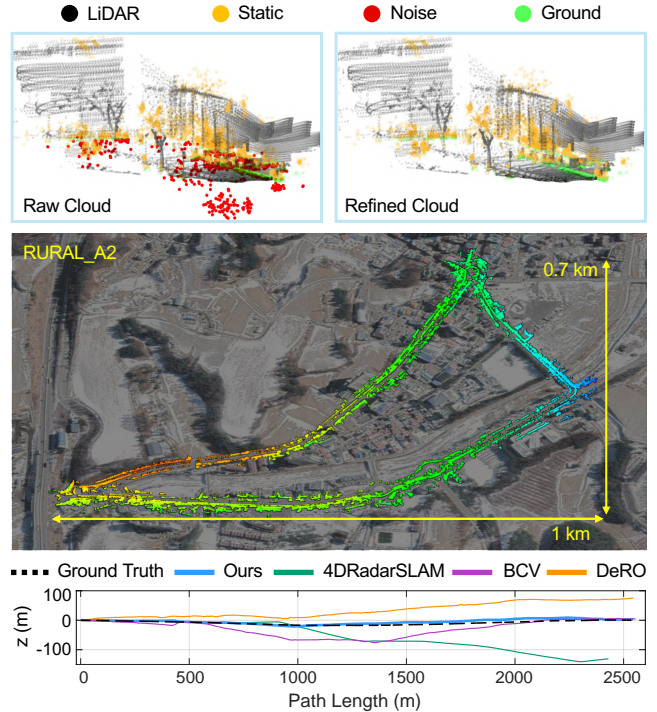


Fig. 1: **Top**: Our uncertainty-aware ground filtering efficiently eliminates the noise (red) from radar. **Middle**: Mapping result of RURAL_A2. Our continuous velocity integration with the Gaussian Process (GP) proficiently handles the sharp turns and roundabouts. **Bottom**: The proposed method shows the lowest elevation error (18m over 2.5km of path length, only 0.72%).

While mitigating inherent noise in radar, estimating 6-degree of freedom (DOF) motion from the 3-DOF linear velocity presents additional challenges. Over the past decades, ego-motion estimation using Doppler velocity has been explored [16–18], and has been extensively advanced to odometry by integrating inertial measurement unit (IMU) [19–23]. In doing so, unfortunately, existing methods overlooked the temporal discrepancies from two sensors, radar and IMU, and the temporal discrepancy in sensor data streams prohibits the tight integration of two sensors for accurate preintegration.

In this paper, we propose a tightly-coupled 4D radar-inertial odometry framework with ground filtering and continuous preintegration for radar-inertial fusion. Existing ground models utilized height thresholding, which struggled with the complexities of slopes and hills. Instead, we use a zone-based approach incorporating the spatial uncertainties from the radar point cloud into ground modeling. Also, radar-inertial fusion is performed through continuous preintegration of velocities. Inspired by IMU preintegration using Gaussian Process (GP) [24], we found that formulating the

radar velocities into GP allows seamless integration with IMU and effectively addresses temporal discrepancies that are often overlooked in existing works. Fig. 1 and Fig. 2 illustrates the improvements and the pipeline of our method. The key contributions are as follows:

- **Uncertainty-Aware Radar Ground Filtering:** Leveraging ground in radar should overcome the ambiguous distribution of the radar point cloud. By associating spatial uncertainties with zone-based ground modeling, we effectively segment out the ground even with its imprecise distributions and secure reliable noise filtering.
- **Novel Continuous Radar Velocity Preintegration:** Effectively mitigating the temporal discrepancies between radar and IMU often disregarded in existing methods. We reformulate radar velocities and IMU using GP for the tightly-coupled preintegration, enabling robust motion estimation directly from the asynchronous measurements without any assumption.
- **Evaluation on Diverse Environmental Conditions:** The proposed method is thoroughly validated on real-world public datasets including high dynamics and harsh weathers, demonstrating robust performance compared to existing 4D radar-inertial odometry algorithms. In particular, our approach achieves substantially enhanced odometry performance in the vertical direction.

II. RELATED WORK

A. Ground-Aided LiDAR and Radar Odometry

The ground is a widely exploited feature for alleviating vertical drift in LiDAR odometry owing to stability and consistency. LeGO-LOAM [8] pioneered the utilization of the ground plane as a planar feature to estimate roll, pitch, and z -axis motion. MULLS [9] integrated the ground plane as a geometric feature within multi-metric matching. Zheng and Zhu [10] leveraged the ground plane for decoupled registration. Chen et al. [11] employed ground segmentation to eliminate redundant features and registration through semantic labeling. GCLO [12] utilized the ground as a planar landmark to mitigate vertical drift. GND-LO [13] achieved 2D motion with planar patches from the ground.

The focus on utilizing ground features in LiDAR odometry has been further extended to radar. Li et al. [14] employed a RANSAC-based ground plane model for noise filtering. DRIO [15] optimized ego-velocity using ground points in single-chip radar. However, these methods relied on heuristic height thresholds to identify ground points, which can be problematic in sloped terrains. To overcome these challenges in radar ground detection, our system incorporates spatial uncertainties from radar with zone-based ground modeling.

B. Radar-Inertial Odometry

Similar to visual and LiDAR odometry, fusion with IMU has shown promising advancements. EKF-RIO [19] fused radar and IMU using extended Kalman filter (EKF) with online calibration, however, the assumption of synchronized measurements was the limitation. Ng et al. [25] proposed a continuous trajectory model on $SE(3)$ to mitigate temporal

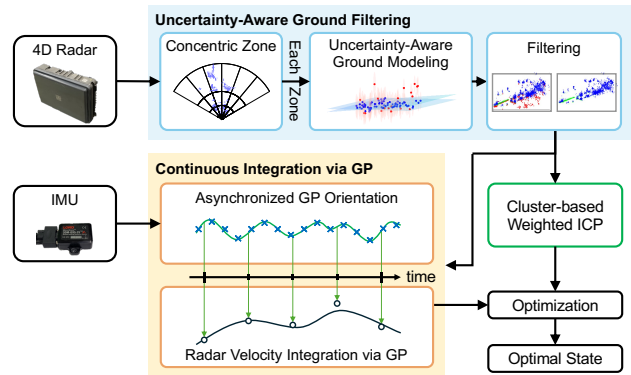


Fig. 2: The overall pipeline of our algorithm.

discrepancies between radar and IMU, yet it encountered z -axis drifts due to high uncertainties on elevation. To address these limitations, Park et al. [20] configured two orthogonal radars to achieve accurate 3D velocity with a velocity factor.

Recent works have integrated spatial information in odometry. Michalczyk et al. [21] proposed EKF-based radar-inertial odometry with Stochastic Cloning. 4D-iRIOM [22] leveraged graduated non-convexity for ego-velocity estimation with scan-to-submap matching via EKF. DeRO [23] utilized the radar velocity in the propagation model with scan matching. Despite these advances, temporal discrepancies between radar and IMU are still overlooked, and unresolved challenges remain concerning the vertical drifts. To tackle these issues, we introduce a continuous radar-inertial fusion framework with GP, which enables assumption-free motion estimation directly from the asynchronous measurements.

III. METHODOLOGY

A. Uncertainty-Aware Radar Ground Filtering

Radar points are prone to degradation due to noise from false alarms and multipath effects, necessitating noise filtering to ensure robustness. We primarily employ radius filtering to eliminate clutter points, and the ground is utilized to mitigate the multipath. To overcome the issues arising from slopes and hills in the existing naive ground fitting, zone-based ground detection is proposed. Considering the conical shape of the radar point cloud, we adopt Concentric Zone Model (CZM) [26], which is characterized by increasing width with distance as depicted in Fig. 3.

The traditional approach for estimating plane models exploited principal component analysis (PCA). Despite their prevalent usage, PCA presents limitations regarding sensitivity to noise and uncertainties, which are crucial for radars. To resolve this, we formulate the plane estimation as an optimization problem that minimizes the sum of Mahalanobis distances between the points and the plane. The Mahalanobis distance from the point p_i to plane is computed as $D_{M_i} = \sqrt{(\mathbf{n}^\top + d)^\top \Sigma_i^{-1} (\mathbf{n}^\top + d)}$, while Σ_i is the associated point-wise covariance matrix, and $[\mathbf{n}, d]$ represents the detected plane model. Then the plane model can be estimated by the subsequent optimization:

$$\underset{[\mathbf{n}, d]}{\operatorname{argmin}} \sum_{i=1}^n D_{M_i}^2 \quad (1)$$

$$\kappa = \mathbf{n}^\top \mathbf{C} \mathbf{n}.$$

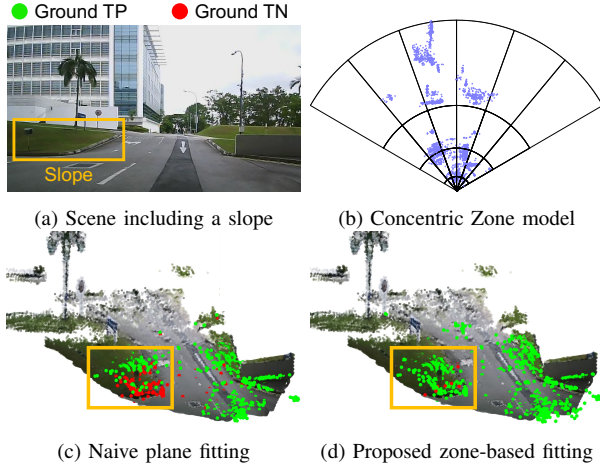


Fig. 3: Comparison between naive plane fitting and our zone-based approach in the sloped environment (yellow box). (c) Many true negatives are found when using naive plane fitting (TN, red). (d) The proposed model effectively filtered ground points even at slope as true positives (TP, green).

$C \in \mathbb{R}^{3 \times 3}$ is the covariance matrix of the point cloud considering spatial uncertainty, and κ means flatness. We merge the points adjacent to the estimated plane and refine the ground set by excluding points that exhibit significant deviations from the plane. These are iterated until the flatness converges in each divided region, and the points below the ground are classified as noise and removed. The entire ground segmentation process is described in Algorithm 1.

After segmentation, the refinement of the height value z_i of the point $p_i = (x_i, y_i, z_i)$ from the ground is performed with the following equation derived from point-wise radial velocity measurement v_{di} [19]:

$$z_i = \frac{V_{xy}v_z - \sqrt{V_{xy}^2v_{di}^2 - (v_{di}^2 - v_z^2)(x_i^2 + y_i^2)v_{di}^2}}{v_{di}^2 - v_z^2}, \quad (2)$$

where v_x, v_y, v_z is the vehicle's ego velocity, and $V_{xy} = v_x x_i + v_y y_i$. The dynamic objects on non-ground points are removed after the refinement process.

Algorithm 1 Uncertainty-aware Ground Segmentation

```

1: Input: PointCloud  $\mathcal{P}$ , sensor height  $h_s, \epsilon_d, \epsilon_f$ ;
2: Output: Ground PointCloud  $\mathcal{G}$ , Static PointCloud  $\mathcal{P}^r$ ;
3: % Divide the pointcloud into each zone.
4:  $\mathcal{P} = \{\mathcal{P}_1, \dots, \mathcal{P}_{N_z}\}, \mathcal{G} = \emptyset, \mathcal{P}^r = \emptyset$ ;
5: for  $i = 1, \dots, N_z$  do
6:   if  $\text{size}(\mathcal{P}_i) > 20$  then
7:     % initialize
8:      $\mathcal{G}_i = \{p_i \in \mathcal{P}_i, \text{s.t. } z_i < -h_s/2\}, \mathcal{Q}_i = \mathcal{P}_i - \mathcal{G}_i$ ;
9:     repeat
10:      estimate the ground plane with  $\mathcal{G}_i$  using (1);
11:       $\mathcal{G}_i \leftarrow \mathcal{G}_i \cup \{p_i \in \mathcal{Q}_i, \text{s.t. } D_{M_i} < \epsilon_d\}$ ;
12:       $\mathcal{Q}_i \leftarrow \mathcal{Q}_i - \{p_i \in \mathcal{Q}_i, \text{s.t. } D_{M_i} < \epsilon_d\}$ ;
13:       $C_i = \text{computeCovariance}(\mathcal{G}_i)$ ;
14:    until  $\text{flatness}(\mathcal{G}_i) < \epsilon_f$ 
15:     $\mathcal{Q}_i \leftarrow \mathcal{Q}_i - \{p_i \in \mathcal{Q}_i, \text{s.t. below the ground}\}$ ;
16:     $\mathcal{G} \leftarrow \mathcal{G} \cup \mathcal{G}_i, \mathcal{P}^r \leftarrow \mathcal{P}^r \cup \mathcal{Q}_i$ ;
17:   end if
18: end for
19: return  $\mathcal{G}, \mathcal{P}^r$ ;

```

B. Continuous Velocity Preintegration via Gaussian Process

Our system leverages a GP-based continuous modeling on radar velocities, seamlessly integrating 4D radar velocity and IMU. Existing radar-inertial odometry approaches have assumed synchronized measurements [19] or employed the discretized propagation model [22] to mitigate temporal discrepancies. Inspired by Le Gentil and Vidal-Calleja [24], who overcome the above limitations in IMU by introducing GP, our work leverages GP for tightly-coupled preintegration of radar velocity and IMU. The continuous nature of the GP resolves the temporal discrepancies and enables direct motion estimation without any assumptions despite the asynchronous data streams between radar velocity and IMU.

Let us briefly summarize [24] and introduce our radar-IMU preintegration formulation. Each component of the time derivative of the rotation vector $\dot{\boldsymbol{\theta}} = (\dot{\theta}_x, \dot{\theta}_y, \dot{\theta}_z)$ is modeled using a zero-mean GP:

$$\dot{\theta}_i(t) \sim \mathcal{GP}(0, k_{\theta_i}(t, t')), \quad (3)$$

where $k_{\theta_i}(t, t')$ is the kernel function and the index i represents x, y, z components each. Then the inference (\star) of the rotation vector is conducted as follows:

$$\begin{aligned} \dot{\theta}_{i\star}(t) &= \mathbf{k}_{\theta_i}(t, \mathbf{t})(\mathbf{K}_{\theta_i}(\mathbf{t}, \mathbf{t}) + \sigma_i^2 \mathbf{I})^{-1} \boldsymbol{\rho}_i \\ \theta_{i\star}(t) &= \int \mathbf{k}_{\theta_i}(t, \mathbf{t})(\mathbf{K}_{\theta_i}(\mathbf{t}, \mathbf{t}) + \sigma_i^2 \mathbf{I})^{-1} \boldsymbol{\rho}_i \partial t \\ \mathbf{k}_{\theta_i}(t, \mathbf{t}) &= [k_{\theta_i}(t, t_1) \dots k_{\theta_i}(t, t_{N_i})] \\ \mathbf{K}_{\theta_i}(\mathbf{t}, \mathbf{t}) &= \begin{bmatrix} k_{\theta_i}(t_1, t_1) & \dots & k_{\theta_i}(t_1, t_{N_i}) \\ \vdots & \ddots & \vdots \\ k_{\theta_i}(t_{N_i}, t_1) & \dots & k_{\theta_i}(t_{N_i}, t_{N_i}) \end{bmatrix}, \end{aligned} \quad (4)$$

$\mathbf{t} = [t_1 \dots t_{N_i}]$ is the vector of the IMU measurement timestamps, $\mathbf{k}_{\theta_i}(t, \mathbf{t})$ is the kernel vector. σ_i is the standard deviation of the IMU gyroscope, and $\boldsymbol{\rho}_i$ is the vector of $\hat{\theta}_i(\mathbf{t})$, which can be achieved with the following optimization:

$$\underset{[\boldsymbol{\rho}_x, \boldsymbol{\rho}_y, \boldsymbol{\rho}_z]}{\text{argmin}} \sum_{n=1}^{N_i} \left(\|e_n^{meas}\|_{\Sigma_\omega}^2 + \|e_n^{gp}\|_{\Sigma_{gp}}^2 \right), \quad (5)$$

where $\|\cdot\|_{\Sigma}$ represents the Mahalanobis norm. The first term, $e_n^{meas} = J_r(\boldsymbol{\theta}_\star(t_n))\dot{\boldsymbol{\theta}}_\star(t_n) - \hat{\boldsymbol{\omega}}(t_n)$ is about the measurement constraint, and Σ_ω is the covariance matrix of IMU gyroscope. The angular velocity is achieved by the chain rule and its right Jacobian $J_r(\boldsymbol{\theta})$ as $\boldsymbol{\omega}(t) = J_r(\boldsymbol{\theta}(t))\dot{\boldsymbol{\theta}}(t)$. Secondly, $e_n^{gp} = \dot{\boldsymbol{\theta}}_\star(t_n) - \hat{\boldsymbol{\theta}}(t_n)$ constrains the unique solution of the optimization with Σ_{gp} being GP variance.

The key idea is that when formulating GP to tightly couple radar and IMU, (4) enables the inference of rotation at any given time, allowing radar-IMU velocity preintegration without additional time synchronization. As the velocity $\mathbf{v} = (v_x, v_y, v_z)$ cannot be modeled with a zero-mean GP, we conduct GP model with the prior mean function $\boldsymbol{\mu}(t)$:

$$v_i(t) \sim \mathcal{GP}(\boldsymbol{\mu}_i(t), k_{v_i}(t, t')). \quad (6)$$

Then the inference of the velocity and translation can be performed as following:

$$v_{i\star}(t) = \boldsymbol{\mu}_i(t) + \mathbf{k}_{v_i}(t, \mathbf{t})(\mathbf{K}_{v_i}(\mathbf{t}, \mathbf{t}) + \epsilon_i^2 \mathbf{I})^{-1} (\boldsymbol{\zeta}_i - \boldsymbol{\mu}_i(\mathbf{t})) \quad (7)$$

$$p_{i\star}(t) = \int \mu_i(t) + \mathbf{k}_{v_i}(t, \mathbf{t})(\mathbf{K}_{v_i}(t, \mathbf{t}) + \epsilon_i^2 \mathbf{I})^{-1} (\zeta_i - \mu_i(\mathbf{t})) \partial t, \quad (8)$$

where ζ_i is the vector of $\hat{v}_i(\mathbf{t})$, $\mathbf{t} = [t_1 \dots t_{N_r}]$ represents the radar timestamps, and ϵ_i is the standard deviation of the velocity measurements. Hence, inducing values ζ_i are achieved by the following optimization:

$$\operatorname{argmin}_{\{\zeta_x, \zeta_y, \zeta_z\}} \sum_{n=1}^{N_r} \left(\|e_n^{meas}\|_{\Sigma_{v_n}}^2 + \|e_n^{gp}\|_{\Sigma_{gp}}^2 \right). \quad (9)$$

Now we have the radar-associated residual as (9) with two residual terms: $e_n^{meas} = \Delta \mathbf{R}^\top \mathbf{v}_\star(t_n) - \tilde{\mathbf{v}}(t_n)$, and $e_n^{gp} = \mathbf{v}_\star(t_n) - \hat{\mathbf{v}}(t_n)$. Here, Σ_{v_n} is the covariance matrix of velocity at timestamp t_n . After (9) has converged, motion increment $\mathbf{T}^{\text{INT}} \in SE(3)$ can be inferred by (4) and (8).

C. Cluster-based Weighted ICP

Although individual radar points exhibit inherent uncertainties, clusters from radar scans can effectively represent the overall shape of structures as shown in Fig. 4. These clusters often correspond to prominent features, which are crucial for accurate scan registration. We utilize the DB-SCAN to segment these clusters and assign higher weights to the correspondences within consistent clusters. Furthermore, the flatness of each cluster is incorporated into the weight calculation, enhancing the spatial representation of each cluster. Therefore, the transformation $\mathbf{T}^{\text{ICP}} \in SE(3)$ between keyframes is estimated by the following optimization:

$$\mathbf{T}^{\text{ICP}} = \operatorname{argmin}_{\mathbf{T}} \sum_i (w_{i,clust} + w_{i,flat}) \|p_i - \mathbf{T}q_i\|_{\Sigma_i}^2 \quad (10)$$

where Σ_i is the covariance matrix including spatial uncertainty, and w_i represents the each weight.

D. Pose Graph Optimization

Incremental motion from §III-B and §III-C is used to define $SE(3)$ edges in the pose graph, and the keyframe-based pose graph optimization is conducted as:

$$\operatorname{argmin}_{\mathbf{X}} \sum_{(i,j)} \|\mathbf{T}_{ij}^{\text{INT}} - h(\mathbf{x}_i, \mathbf{x}_j)\|_{\Sigma_{\text{INT}}}^2 + \|\mathbf{T}_{ij}^{\text{ICP}} - h(\mathbf{x}_i, \mathbf{x}_j)\|_{\Sigma_{\text{ICP}}}^2 \quad (11)$$

where $h(\mathbf{x}_i, \mathbf{x}_j)$ computes the relative transformation between two poses. A new keyframe is selected when the motion increment from numerical integration exceeds a pre-defined threshold relative to the previous keyframe. The *g2o* [27] library is utilized for back-end optimization.

IV. EXPERIMENT

A. Datasets and Evaluation Metric

For evaluation, we use NTU4DRadLM [28] and MSC-RAD4R [29] datasets, both utilized Oculii Eagle 4D radar and IMU. NTU4DRadLM is designed to assess performance in semi-structured environments with ground vehicle systems. MSC-RAD4R includes urban and rural environments using a car platform with fast and high-dynamic sequences.

We benchmark our method against state-of-the-art open-sourced 4D radar and radar-inertial odometry algorithms: APD-GICP in 4DRadarSLAM [30], EKF-RIO [19] BCV

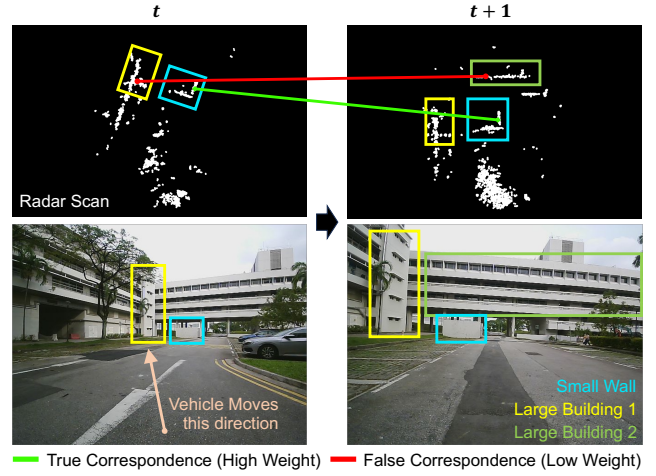


Fig. 4: As the vehicle moves t to $t+1$, prominent features maintain the structures in radar (yellow, cyan). The higher weight is allocated to correspondences within the consistent cluster (green line).

[20], and DeRO [23]. Unfortunately, other ground-aided radar-inertial odometry [14, 15] are not open-sourced for comparison. Instead, a thorough comparative analysis for our uncertainty-aware ground filtering will be provided in §IV-D. We remove the loop closure in 4DRadarSLAM to ensure equitable comparison, as our approach focuses solely on odometry. For quantitative analysis, we compute the root mean square error (RMSE) of the Absolute Trajectory Error (ATE) and Relative Pose Error (RPE) with *evo* library [31]. ATE is expressed in meters, and RPE is expressed in degrees per meter and percentage for the rotational (RPE_r) and translational (RPE_t) components, respectively. Since MSC-RAD4R provides ground truth data only for translation, we evaluated only the ATE in MSC-RAD4R. In each table, we highlight the best results in **bold**.

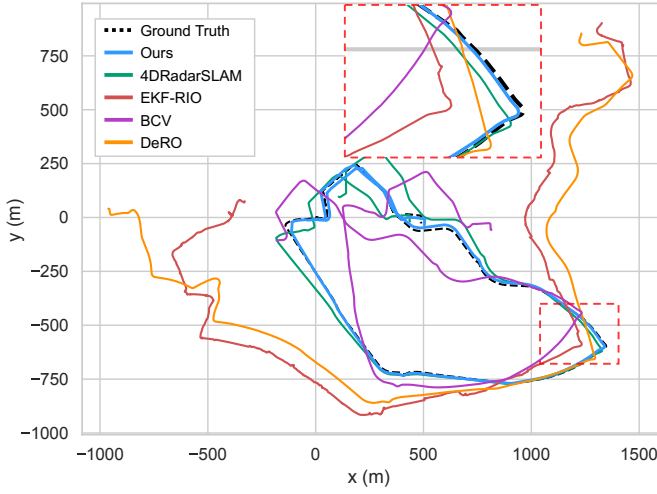
B. Evaluation on the NTU4DRadLM Dataset

As detailed in Table. I, our method represents consistent performance through the experiments. In the cases of `ny1` and `loop2`, where noise generated by sunshades or ceilings is prevalent, 4DRadarSLAM encounters performance degradation induced by the absence of effective noise filtering. Despite this, our method exhibits robust performance owing to ground filtering. `loop2` involves vigorous rotational movements, discretized propagation model in EKF-RIO and BCV struggled from orientation estimation as illustrated in Fig. 5a. DeRO exhibits the worst performance, affected by both noise and discretization. Conversely, our continuous model with GP enables accurate estimation throughout the experiments, demonstrating that the proposed method effectively handles the aforementioned challenges.

Interestingly, 4DRadarSLAM achieves the lowest ATE in `loop3` even without utilizing IMU. The `loop3` sequence includes vertical structures such as walls and hills, which generate horizontal multipath. Our filtering process, which focuses on rejecting underground outliers, is less effective for these types of noise. Nevertheless, our method exhibits the lowest RPE_r , validating the effectiveness of continuous integration as shown in Table. II and Fig. 5b.

TABLE I: ATE (m) Evaluation Results in NTU4DRadLM and MSC-RAD4R (Best results in **bold**)

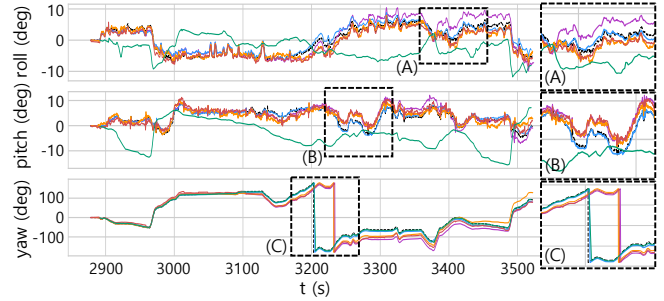
Method	cp	nyl	loop2	loop3	URBAN_A0	LOOP_A0	LOOP_B0	LOOP_C0	LOOP_D0	LOOP_E0	RURAL_A2	RURAL_B2
4DRadarSLAM [30]	0.768	7.574	131.948	26.755	16.097	110.269	88.228	14.333	19.984	56.347	33.256	24.251
EKF-RIO[19]	6.241	58.913	436.262	181.422	18.638	96.662	159.662	176.106	26.895	196.652	278.788	251.471
BCV[20]	3.163	41.002	222.182	231.449	2.667	120.297	130.256	81.444	75.382	95.018	19.423	14.256
DeRO[23]	4.910	48.275	438.643	146.659	12.317	149.277	39.620	51.058	46.708	186.376	263.003	73.784
Proposed	0.699	5.009	42.185	28.269	1.757	6.752	9.884	6.450	4.280	35.266	9.480	10.927



(a) Estimated trajectory in loop2

TABLE II: RPE (Trans (%)/Rot (deg/m)) in NTU4DRadLM

Method	cp	nyl	loop2	loop3
4DRadarSLAM	0.106/1.107	0.178/1.106	0.745/0.751	0.472/0.562
EKF-RIO	0.298/1.806	0.423/1.864	1.750/1.179	1.307/0.596
BCV	0.096/1.232	0.142/0.949	0.368/0.564	0.546/0.537
DeRO	0.112/1.625	0.318/1.610	2.059/0.880	0.373/0.524
Proposed	0.085/0.722	0.116/1.003	0.338/0.547	0.365/0.384

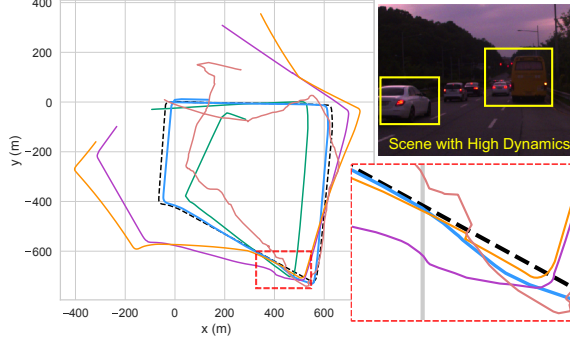


(b) Estimated rotation in loop3 (degrees)

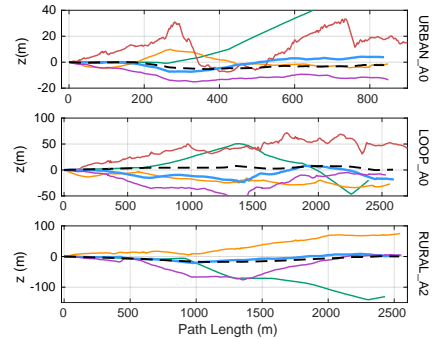
Fig. 5: (a) The trajectory plots of loop2 in NTU4DRadLM. The proposed method (blue) best aligns with the ground truth (black). (b) Estimated rotation in loop3. In terms of heading (a zoomed view ‘C’ in (b)), both 4DRadarSLAM and ours demonstrate superior performance; however, including the roll and pitch, ours exhibits better results (zoomed views ‘A’ and ‘B’ in (b)).



(a) Map based on odometry



(b) Estimated trajectory in LOOP_A0



(c) Elevation over traveled path length (m)

Fig. 6: (a) Qualitative analysis of the proposed odometry in LOOP_A0. Point cloud map based on our odometry shows well-alignment with the satellite image. (b) Sudden ego-velocity drift can occur due to large dynamic objects in LOOP_A0. While other radar-inertial baselines fail to generate accurate trajectories, our method effectively handles the challenging scenarios. (c) Detailed analysis in elevation on URBAN_A0, LOOP_A0, RURAL_A2, respectively. In RURAL_A2, EKF-RIO is omitted for clarity.

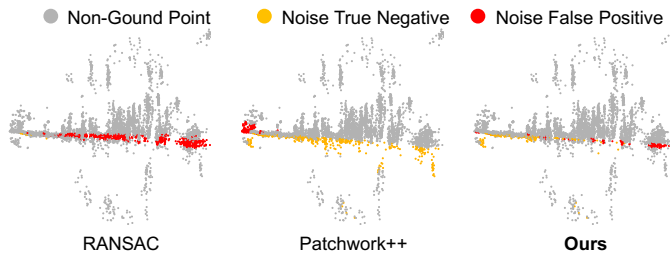
C. Evaluation on the MSC-RAD4R Dataset

In MSC-RAD4R, our method outperforms the other baselines as represented in Table. I. URBAN_A0 is characterized by numerous street trees, resulting in dominant vertical line features. These features are incompatible with point-to-plane errors in 4DRadarSLAM, causing localization failure. In the LOOP sequences, which involve high vehicle speed with rapid rotational movements, 4DRadarSLAM indicates the scale misalignment. As shown in Fig. 6, large dynamic objects can produce abrupt drifts in ego-velocity estimation. Discretized propagation models that rely on constant state assumptions exacerbate these errors, as illustrated in the performance of BCV and DeRO. Nonetheless, the proposed algorithm demonstrates consistent performance benefiting from reliance on the GP-based continuous model, which effectively compensates for these measurement drifts and

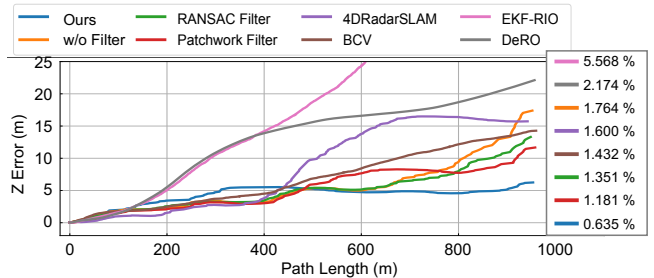
results in a smooth trajectory. RURAL_A2 and RURAL_B2 are characterized by sharp roundabouts and high dynamics in harsh weather conditions, presenting significant challenges. Nonetheless, our algorithm maintains reliable performance. Remarkably, 4DRadarSLAM achieves comparable results without leveraging IMU, underscoring the appropriate fusion model for asynchronous sensor measurements. Throughout the experiments, we observe that our methodology exhibits minimal elevation error.

D. Effect of Uncertainty-Aware Ground Filtering

In the following analysis (§IV-D-§IV-E), we denote our system as FULL, uncertainty-aware ground filtering as FILTER, and continuous velocity preintegration as CONT. We perform ablation studies to verify the effect of each module, compared to discrete integration without any noise filtering method (RAW).



(a) Noise filtering result of each method in `ny1`



(b) z -axis error in `ny1`

Fig. 7: (a) Qualitative results of each filtering method projected onto the XZ -plane. The ground truth of the noise was created by projecting the LiDAR scan onto the radar. (b) The effect of each outlier rejection in z -axis odometry. Vertical errors over path length are detailed in the right box.

TABLE III: Effect of Each Module in ATE

	RAW	CONT	FILTER	FULL
<code>cp</code>	2.337	1.307	2.029	0.699
<code>ny1</code>	26.319	19.069	5.888	5.009
<code>URBAN_A0</code>	13.433	2.163	12.412	1.757
<code>LOOP_A0</code>	101.956	23.345	84.664	16.752
<code>RURAL_A2</code>	76.799	20.764	47.966	9.480

To evaluate the effectiveness of our filtering method, we conduct a comparative analysis with the RANSAC-based naive plane fitting [14] and Patchwork++ [26]. The qualitative results are depicted in Fig. 7a. The RANSAC-based approach exploits height thresholding for ground point segmentation; however, this produces false positives in areas with varying terrain elevation, such as slopes, resulting in the erroneous classification of significant static features as noise. Patchwork++ fails to account for spatial uncertainties associated with distant points, yielding unmitigated noise despite utilizing zone-based ground segmentation. In contrast, our method accurately filters out the noises.

Fig. 7b indicates that our approach outperforms other methods over elevation accuracy. Table. III presents the quantitative improvements in ATE attributed to our filtering method. As expected, RAW shows diminished performance compared to FILTER due to the absence of noise filtering, demonstrating the robustness of our filtering approach in varying conditions. These improvements are particularly significant in the `ny1` dataset, where the majority of noise consists of underground noise caused by sunshades. This denotes that our method is highly effective in mitigating this predominant type of noise. In conclusion, our uncertainty-aware ground model effectively handles noises and enhances the odometry accuracy.

E. Effect of Continuous Velocity PreIntegration

In Table. III, FULL demonstrates superior performance over RAW and FILTER, both numerically integrate the IMU angular velocity and the radar velocity [32]. The discretized propagation model to address the temporal discrepancies exhibits limitations due to measurement drift and constant state assumptions, resulting in significant degradation on LOOP_A0 and RURAL_A2 with high vehicle speeds and sharp turns. Conversely, FULL effectively accommodates

TABLE IV: Computation Time of Each Module (ms)

	Ego-vel	Ground	Scan Matching	GP Integration	Optimization
<code>loop2</code>	0.31	68.38	2.87	615.43	370.45
<code>LOOP_A0</code>	0.99	52.67	2.05	789.77	436.77

vigorously changing orientations and velocities, attributed to the proposed velocity preintegration, which enables direct motion estimation through asynchronous IMU angular velocities and radar velocities. Moreover, the smoothness nature of GP makes our preintegration process more robust to unavoidable measurement noise.

F. Computational Cost

The time consumption analysis results in `loop2` and `LOOP_A0`, which represent the longest paths in the dataset, are presented in Table. IV. The experiments were conducted on Intel i7 CPU@2.50 GHz and 64 GB RAM. Uncertainty-aware ground filtering and scan matching can be executed in real-time. While GP integration and optimization are computationally expensive, they are performed in parallel in the back-end, ensuring that our system maintains real-time capability. Moreover, additional performance enhancements can be pursued during continuous preintegration.

V. CONCLUSION

In this paper, we present a tightly-coupled 4D-radar-inertial odometry framework. By employing uncertainty-aware ground filtering, we effectively eliminate the inherent noises from radar. Continuous velocity preintegration via GP effectively mitigates temporal discrepancies between radar and IMU, and enables robust motion estimation directly from the asynchronous measurements without any assumptions. We have demonstrated that our method outperforms existing 4D radar-inertial odometry algorithms in terms of precision and resilience across various scenarios through the public datasets. Notably, the proposed algorithm achieves substantially enhanced vertical odometry accuracy.

Despite significant advancements, minor challenges remain. Since our filtering process primarily targets underground noise, horizontal multipath remains a concern. For future work, we aim to incorporate vertical plane modeling to enhance the robustness of the odometry and mapping system. Also, we plan to improve our system by developing a comprehensive bias model for the IMU gyroscope or incorporating the accelerometer measurements.

REFERENCES

- [1] K. Harlow, H. Jang, T. D. Barfoot, A. Kim, and C. Heckman, "A New Wave in Robotics: Survey on Recent mmWave Radar Applications in Robotics," *IEEE Trans. Robot.*, 2024, accepted. To appear.
- [2] N. J. Abu-Alrub and N. A. Rawashdeh, "Radar Odometry for Autonomous Ground Vehicles: A Survey of Methods and Datasets," *IEEE Trans. Intell. Vehicles*, vol. 9, no. 3, pp. 4275–4291, 2024.
- [3] J. W. Starr and B. Y. Lattimer, "Evaluation of Navigation Sensors in Fire Smoke Environments," *Fire Technology*, vol. 50, pp. 1459–1481, 2014.
- [4] M. Bijelic, T. Gruber, and W. Ritter, "A Benchmark for Lidar Sensors in Fog: Is Detection Breaking Down?" in *Proc. IEEE Intell. Vehicle Symposium*. IEEE, 2018, pp. 760–767.
- [5] A. Kramer and C. Heckman, "Radar-inertial state estimation and obstacle detection for micro-aerial vehicles in dense fog," in *Experimental Robotics: The 17th International Symposium*. Springer, 2021, pp. 3–16.
- [6] M. Nissov, N. Khedekar, and K. Alexis, "Degradation Resilient LiDAR-Radar-Inertial Odometry," *arXiv preprint arXiv:2403.05332*, 2024.
- [7] D. Adolfsson, M. Magnusson, A. Alhashimi, A. J. Lilienthal, and H. Andreasson, "Lidar-Level Localization With Radar? The CFEAR Approach to Accurate, Fast, and Robust Large-Scale Radar Odometry in Diverse Environments," *IEEE Trans. Robot.*, vol. 39, no. 2, pp. 1476–1495, 2023.
- [8] T. Shan and B. Englot, "LeGO-LOAM: Lightweight and Ground-Optimized Lidar Odometry and Mapping on Variable Terrain," in *Proc. IEEE/RSJ Intl. Conf. on Intell. Robots and Sys.* IEEE, 2018, pp. 4758–4765.
- [9] Y. Pan, P. Xiao, Y. He, Z. Shao, and Z. Li, "MULLS: Versatile LiDAR SLAM via Multi-metric Linear Least Square," in *Proc. IEEE Intl. Conf. on Robot. and Automat.*, 2021, pp. 11 633–11 640.
- [10] X. Zheng and J. Zhu, "Efficient LiDAR odometry for Autonomous Driving," *IEEE Robot. and Automat. Lett.*, vol. 6, no. 4, pp. 8458–8465, 2021.
- [11] P. Chen, W. Shi, S. Bao, M. Wang, W. Fan, and H. Xiang, "Low-Drift Odometry, Mapping and Ground Segmentation Using a Backpack LiDAR System," *IEEE Robot. and Automat. Lett.*, vol. 6, no. 4, pp. 7285–7292, 2021.
- [12] X. Wei, J. Lv, J. Sun, E. Dong, and S. Pu, "GCLO: Ground Constrained LiDAR Odometry with Low-drifts for GPS-denied Indoor Environments," in *Proc. IEEE Intl. Conf. on Robot. and Automat.* IEEE, 2022, pp. 2229–2235.
- [13] A. Galeote-Luque, J.-R. Ruiz-Sarmiento, and J. Gonzalez-Jimenez, "GND-LO: Ground Decoupled 3D Lidar Odometry Based on Planar Patches," *IEEE Robot. and Automat. Lett.*, vol. 8, no. 11, pp. 6923–6930, 2023.
- [14] X. Li, H. Zhang, and W. Chen, "4D Radar-Based Pose Graph SLAM With Ego-Velocity Pre-Integration Factor," *IEEE Robot. and Automat. Lett.*, vol. 8, no. 8, pp. 5124–5131, 2023.
- [15] H. Chen, Y. Liu, and Y. Cheng, "DRIO: Robust Radar-Inertial Odometry in Dynamic Environments," *IEEE Robot. and Automat. Lett.*, vol. 8, no. 9, pp. 5918–5925, 2023.
- [16] D. Kellner, M. Barjenbruch, J. Klappstein, J. Dickmann, and K. Dietmayer, "Instantaneous ego-motion estimation using Doppler radar," in *Proc. IEEE Intell. Transport. Sys. Conf.* IEEE, 2013, pp. 869–874.
- [17] A. Kramer, C. Stahoviak, A. Santamaria-Navarro, A.-A. Agha-Mohammadi, and C. Heckman, "Radar-Inertial Ego-Velocity Estimation for Visually Degraded Environments," in *Proc. IEEE Intl. Conf. on Robot. and Automat.* IEEE, 2020, pp. 5739–5746.
- [18] K. Haggag, S. Lange, T. Pfeifer, and P. Protzel, "A Credible and Robust Approach to Ego-Motion Estimation Using an Automotive Radar," *IEEE Robot. and Automat. Lett.*, vol. 7, no. 3, pp. 6020–6027, 2022.
- [19] C. Doer and G. F. Trommer, "Radar inertial odometry with on-line calibration," in *European Navigation Conference (ENC)*, 2020, pp. 1–10.
- [20] Y. S. Park, Y.-S. Shin, J. Kim, and A. Kim, "3D ego-Motion Estimation Using low-Cost mmWave Radars via Radar Velocity Factor for Pose-Graph SLAM," *IEEE Robot. and Automat. Lett.*, vol. 6, no. 4, pp. 7691–7698, 2021.
- [21] J. Michalczyk, R. Jung, and S. Weiss, "Tightly-Coupled EKF-Based Radar-Inertial Odometry," in *Proc. IEEE/RSJ Intl. Conf. on Intell. Robots and Sys.* IEEE, 2022, pp. 12 336–12 343.
- [22] Y. Zhuang, B. Wang, J. Huai, and M. Li, "4D iRIOM: 4D Imaging Radar Inertial Odometry and Mapping," *IEEE Robot. and Automat. Lett.*, vol. 8, no. 6, pp. 3246–3253, 2023.
- [23] H. V. Do, Y. H. Kim, J. H. Lee, M. H. Lee, and J. W. Song, "DeRO: Dead Reckoning Based on Radar Odometry With Accelerometers Aided for Robot Localization," in *Proc. IEEE/RSJ Intl. Conf. on Intell. Robots and Sys.* IEEE, 2024, accepted. To appear.
- [24] C. Le Gentil and T. Vidal-Calleja, "Continuous Integration over SO (3) for IMU Preintegration," *Proc. Robot.: Science & Sys. Conf.*, 2021.
- [25] Y. Z. Ng, B. Choi, R. Tan, and L. Heng, "Continuous-time Radar-inertial Odometry for Automotive Radars," in *Proc. IEEE/RSJ Intl. Conf. on Intell. Robots and Sys.* IEEE, 2021, pp. 323–330.
- [26] S. Lee, H. Lim, and H. Myung, "Patchwork++: Fast and Robust Ground Segmentation Solving Partial Under-Segmentation Using 3D Point Cloud," in *Proc. IEEE/RSJ Intl. Conf. on Intell. Robots and Sys.*, 2022, pp. 13 276–13 283.
- [27] R. Kümmerle, G. Grisetti, H. Strasdat, K. Konolige, and W. Burgard, "G2o: A general framework for graph optimization," in *Proc. IEEE Intl. Conf. on Robot. and Automat.* IEEE, 2011, pp. 3607–3613.
- [28] J. Zhang, H. Zhuge, Y. Liu, G. Peng, Z. Wu, H. Zhang, Q. Lyu, H. Li, C. Zhao, D. Kircali, S. Mharolkar, X. Yang, S. Yi, Y. Wang, and D. Wang, "NTU4DRadLM: 4D Radar-Centric Multi-Modal Dataset for Localization and Mapping," in *Proc. IEEE Intell. Transport. Sys. Conf.* IEEE, 2023, pp. 4291–4296.
- [29] M. Choi, S. Yang, S. Han, Y. Lee, M. Lee, K. H. Choi, and K.-S. Kim, "MSC-RAD4R: ROS-Based Automotive Dataset With 4D Radar," *IEEE Robot. and Automat. Lett.*, vol. 8, no. 11, pp. 7194–7201, 2023.
- [30] J. Zhang, H. Zhuge, Z. Wu, G. Peng, M. Wen, Y. Liu, and D. Wang, "4DRadarSLAM: A 4D Imaging Radar SLAM System for Large-scale Environments based on Pose Graph Optimization," in *Proc. IEEE Intl. Conf. on Robot. and Automat.* IEEE, 2023, pp. 8333–8340.
- [31] M. Grupp, "Evo: Python package for the evaluation of odometry and slam," <https://github.com/MichaelGrupp/evo>, 2017.
- [32] V. Kubelka, E. Fritz, and M. Magnusson, "Do we need scan-matching in radar odometry?" in *Proc. IEEE Intl. Conf. on Robot. and Automat.* IEEE, 2024, pp. 13 710–13 716.